stellarator news

Published by Fusion Energy Division, Oak Ridge National Laboratory
Building 9201-2 P.O. Box 2009 Oak Ridge, TN 37831-8071, USA

Editor: James A. Rome Issue 52 July 1997
E-Mail: jar@ornl.gov Phone (423) 574-1306 Fax: (423) 241-6211
On the Web at *http://www.ornl.gov/fed/stelnews*

*J** transport optimization of low-aspect-ratio stellarators

I. Introduction

Low-aspect-ratio, modular, tilted-coil stellarators [1–5] offer the attractive features of compact steady-state fusion power systems, high volume utilization, axisymmetric diverted regions, and the absence of low-order resonances (leading to islands) near the plasma edge. However, recent studies of confinement [3] in these devices have indicated the need for further transport optimization.

Of the two quasisymmetric approaches, only quasitoroidal optimizations have successfully been achieved [6] at low aspect ratio. The quasihelical approach [7] is expected to be applicable only at higher aspect ratios [8]. However, in parallel with the quasisymmetric approaches, various techniques for directly reducing the particle drifts away from magnetic flux surfaces have also been developed. Initial work [9] focused on improving the confinement of deeply trapped particles, since these orbits could be simply related to contours of the minimum of $|\boldsymbol{B}|$ along the toroidal direction.

We have developed a more general approach that improves the alignment of the approximate second adiabatic invariant [10,11] J^* contours with magnetic flux surfaces. This approach allows confinement improvement over the entire trapped particle population as well as a possible reduction in the number of transitional particles. Such an approach is equivalent to bounce-averaged omnigeneity, which has recently been interpreted [12–14] in terms of equal spacing of $|\boldsymbol{B}|$ contours on a magnetic flux surface. These methods are expected to open up a wider design space than the previous quasisymmetry approaches, since they place a weaker constraint on the form of the $|\boldsymbol{B}|$ spectrum. Besides improving confinement at low aspect ratio, this additional flexibility could allow for simultaneous optimization with respect to stability, bootstrap currents, and other physics criteria. We present an example of using the concept of bounce-averaged omnigeneity to generate an actual low-aspect-ratio stellar-

In this issue . . .

J^* transport optimization of low-aspect-ratio stellarators
Significant confinement improvements have been achieved in low-aspect-ratio stellarator/tokamak hybrid configurations by aligning the J^* contours with the flux surfaces. 1

First experimental results in TJ-II flexible heliac: Magnetic surface mapping
Measurements agree well with predictions if low-order rational surfaces are excluded. 7

Design and construction of the SC current transmission system for the LHD
Nine sets of superconducting (SC) bus lines were installed in the Large Helical Device. The total length of the SC bus lines is 497 m. Design concepts and construction status are presented. 8

Construction of the cryogenic system for the LHD
The cryogenic system for the Large Helical Device consists of the helium refrigerator/liquefier, the LHD cryostat, and the peripheral equipment, such as superconducting bus lines, control valve boxes, cryogenic transfer tubes, etc. The assembling of the LHD cryogenic system is now at the final stage and will be completed at the end of 1997. 10

Cornerstone placed for the Greifswald branch of IPP Garching
The cornerstone for the Greifswald Branch of IPP Garching was placed on 19 June 1997. 12

Recent Helias reactor study developments
Recent results of Helias reactor studies are described, highlighting the coil system, finite-beta equilibrium, neoclassical transport, alpha particle studies, and ignition scenarios. 13

Meeting announcements 16

All opinions expressed herein are those of the authors and should not be reproduced, quoted in publications, or used as a reference without the author's consent.
Oak Ridge National Laboratory is managed by Lockheed Martin Energy Research Corporation for the U.S. Department of Energy.

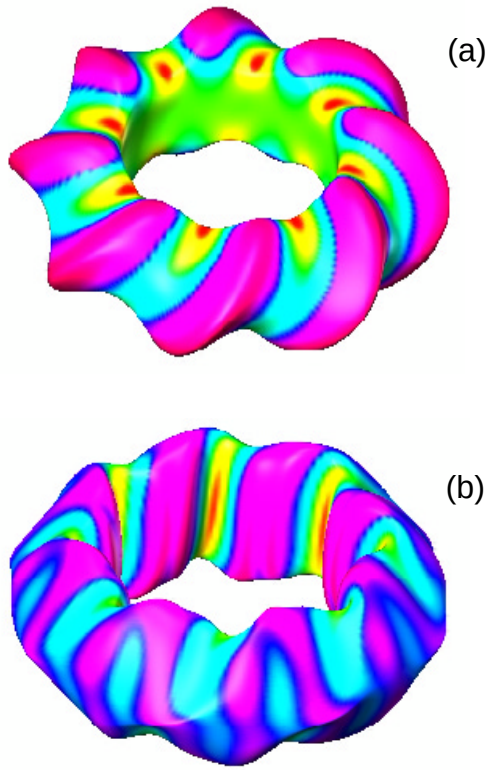

Fig. 1. Outer flux surface shape with color contours proportional to $|\boldsymbol{B}|$ magnitude for (a) an unoptimized configuration and (b) a J^*-optimized configuration.

ator configuration. We first describe our new optimization procedure and then analyze both the thermal and energetic particle transport properties of the optimized configuration. We find that sizable reductions (factors of 20–30) in thermal particle transport rates can be achieved along with a closing off of the loss cone for more energetic particles. Examination of the $|\boldsymbol{B}|$ spectrum indicates that the optimized state is neither purely quasihelical nor quasitoroidal.

Description of the Optimization Procedure

Our approach uses the VMEC three-dimensional (3-D) magnetohydrodynamic (MHD) equilibrium solver [15] as the inner physics evaluation loop of a Levenberg-Marquardt optimizer. The control variables are the shape of the outermost magnetic flux surface, which is expressed in terms of about 10 Fourier harmonics of both R and z, and the plasma current profile (in the case of stellarator/tokamak hybrids). Typically, the optimization targets used are the following: alignment of B_{min}, B_{max}, and J^* constant surfaces with magnetic flux contours; matching of $\tau(\psi)$ to a specified rotational transform profile; maintenance of a magnetic well over most of the plasma cross section; $R_0/a \approx 3$; avoidance of strongly curved segments on the flux surface; and minimization of magnetic ripple. Here B_{min} and B_{max} are the two-dimensional (2-D) functions of ψ and θ which are formed by recording the minimum/maximum value of $|\boldsymbol{B}|$ along the toroidal direction within a single field period at fixed ψ, θ. For the examples given here, the alignment of the B_{min}, B_{max}, and trapped J^* contours with ψ is typically carried out over three flux surfaces and, additionally for J^*, at four values of the pitch angle variable ε/μ. Each of the target functions is multiplied by an associated weight and summed to form a single χ^2 functional, which is to be minimized. The initial condition on the outer flux surface shape is derived from a free-boundary VMEC equilibrium based on a known set of coils.

Once a satisfactorily optimized outer flux surface is found, we vary a parameterized set of coils in order to match $\boldsymbol{B}$ at the outer flux surface [16]. In general, this is not a unique process [17] and multiple solutions are possible, depending on the number of coils per field period, the winding surface, etc. By separating the physics and coil optimizations into separate steps, efficiency is gained and a better understanding of the trade-offs of each phase of the design process is possible. We discuss only the physics (i.e., outer flux surface) optimization.

This optimization technique has been applied to an 8-field-

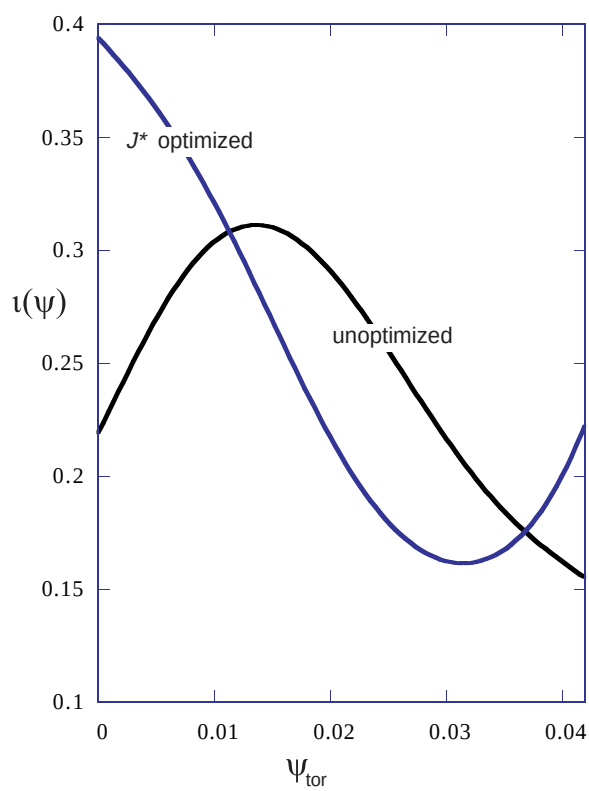

Fig. 2. Rotational transform profiles in unoptimized and J^* optimized configurations.

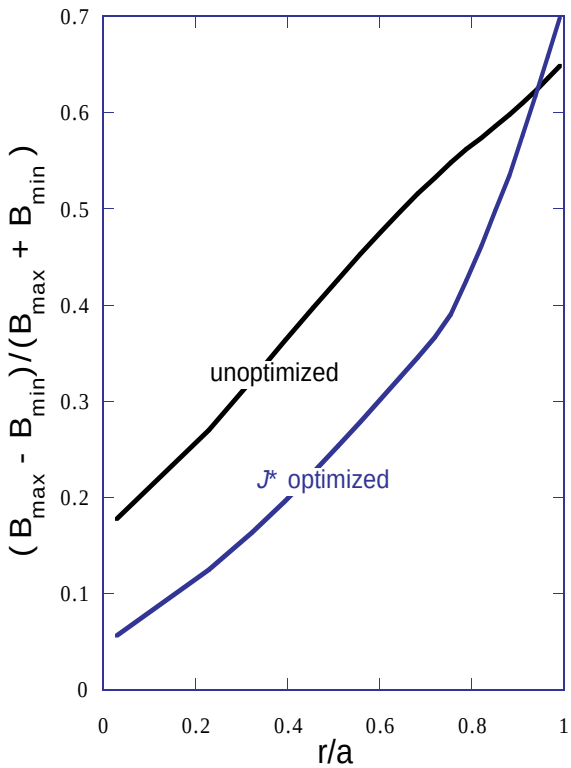

Fig. 3. Ripple strength $(B_{max} - B_{min})/(B_{max} + B_{min})$ profile for unoptimized and J^*-optimized configurations.

period, hybrid stellarator/tokamak device with major radius $R_0 = 1.4$ m, $B_{axis} = 1.2$ T, $R_0/a \approx 3$, $\langle\beta\rangle = 2\%$, and a plasma current of around 60 kA. We compare the initial unoptimized device, whose flux surface shape was determined by a set of eight external modular coils, with an optimized configuration based on the alignment of J^* with ψ. Figure 1 shows 3-D rendered flux surfaces for the two configurations with color shading to indicate the constant $|\boldsymbol{B}|$ contours.

The profiles of τ and $(B_{max} - B_{min})/(B_{max} + B_{min})$ (related to ripple strength) are shown in Figs. 2 and 3. The unoptimized case has a central region of reversed shear, while the optimized case tends to have edge reversed shear regions. The optimized case also has lower levels of ripple near the magnetic axis. In Figs. 4(a) and 4(b) the B_{min} contours show that the unoptimized configuration (a) has completely unclosed B_{min} contours (which means that all deeply trapped particles are lost), while the optimized configuration (b) has large regions of closed B_{min} contours. We have also examined the J^* contours over a range of pitch angles and find that they are more closely aligned with flux surfaces than in the original configuration.

As mentioned earlier, the J^* optimization process leads to configurations that are neither quasitoroidal nor quasi-

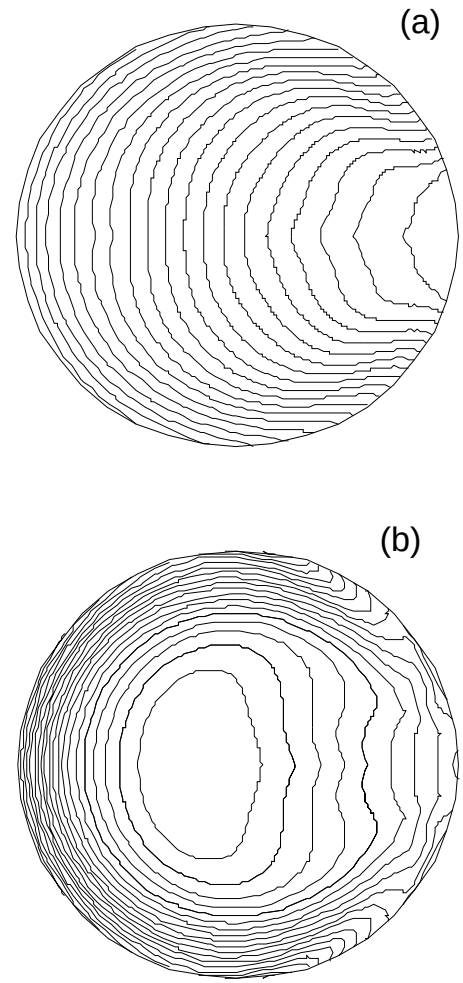

Fig. 4. B_{min} contours for (a) unoptimized and (b) J^*-optimized configurations.

helical. This is demonstrated in Figs. 5(a) and 5(b), where the B_{mn} spectra (excluding the $m = 0$, $n = 0$ mode) are plotted vs magnetic flux for (a) the unoptimized case and (b) the J^*-optimized case. Although the spread of the higher order modes has been reduced in Fig. 5(b), it still contains significant $n \neq 0$ terms and a mixture of different helicities.

The approach to bounce-averaged omnigeneity through the alignment of trapped-particle J^* surfaces with flux surfaces should be approximately equivalent to the criterion of equal angular separation between constant $|\boldsymbol{B}|$ contours on a flux surface, suggested recently in Refs. [12–14]. The differences between these criteria are of order τ/N (N = number of field periods) owing to the use of the exact J (integral along a field line) and J^* (integral along ϕ_{Boozer}) and are generally small for the configuration examined here. We have confirmed this by plotting contours of equal toroidal angle separation between a range of $|\boldsymbol{B}|$ values and find that these contours are very similar to those of the

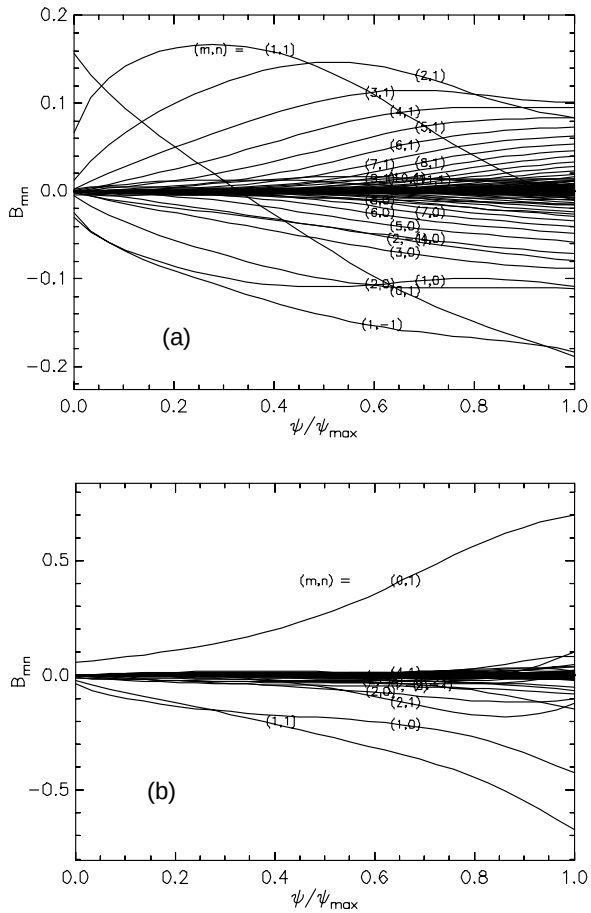

Fig. 5. B_{mn} spectrum vs toroidal magnetic flux for (a) unoptimized and (b) J^*-optimized configurations.

equivalent J^* surfaces (i.e., at $\varepsilon/\mu = |B|$).

Confinement Properties of the Optimized Configurations

Thermal Transport

In order to compare the thermal transport of the configurations presented in the previous section, we have chosen to follow the Monte Carlo evolution [18] of 256 particles started at a single radial location with a random distribution in pitch angle and in poloidal and toroidal angles and with a Maxwellian distribution in energy. The background plasma has a density of 5×10^{13} cm^{-3}, and both the background and test particle distributions have a temperature of 1 keV. The same random number seed was used for each configuration so that initial conditions are equivalent. We monitor the escape of particles and energy through the outer flux as a function of time and use this as our basic measure of thermal confinement. This loss rate has the advantage of including both the direct prompt orbit losses and diffusive losses, and it involves no assumptions regarding localized transport. A variety of other measures

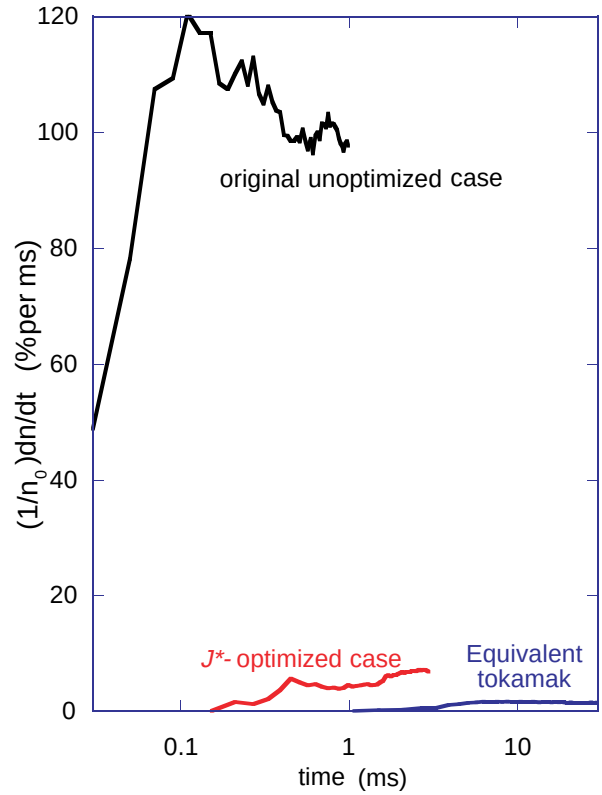

Fig. 6. Monte Carlo particle loss rates through the last closed flux surface vs time for original unoptimized configuration, J^*-optimized configuration, and an equivalent tokamak.

of thermal transport are under consideration and development.

In Fig. 6 we show the particle loss rates vs time for the original and J^*-optimized cases and for an equivalent tokamak case. The latter configuration is arrived at by taking the J^*-optimized case and retaining only the $n = 0$ harmonics. Although not all of these simulations may have reached steady state, they clearly demonstrate that the optimization procedure can substantially reduce loss rates, leading roughly to a factor of 20–30 reduction over the initial unoptimized configuration. Loss rates for the J^*-optimized case are also within a factor of 3–4 of the equivalent tokamak loss rates.

Energetic Particle Transport

The confinement of collisionless energetic particles is one of the primary motivations for the optimizations discussed here since the thermal particle confinement can, in principle, also be improved by control of the ambipolar electric field. Because most heating schemes rely on some form of energetic particle tail population, heating efficiencies can depend sensitively on the confinement of this species. As indicated in Fig. 4, the deeply trapped particles are generally promptly lost in the unoptimized configuration; as a

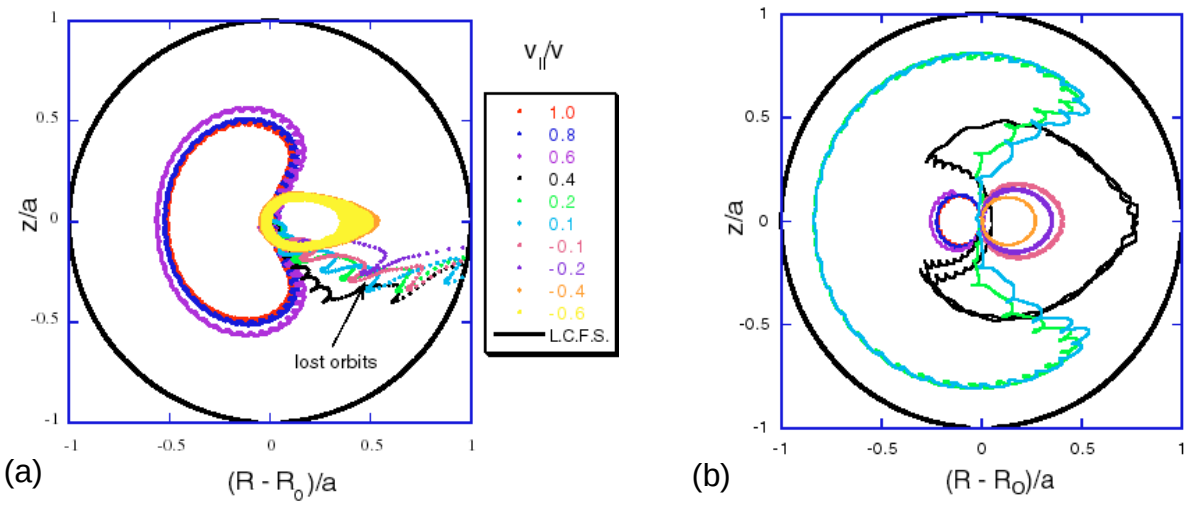

Fig. 7. Energetic 40-keV ion orbit trajectories in (a) the original unoptimized configuration and (b) the J^*-optimized configuration for orbits passing through the magnetic axis over a color-coded range of initial pitch angles ($v_{||}/v$ = –0.6, –0.4, –0.2, 0.1, 0.2, 0.4, 0.6, 0.8, 1.0).

result of the large level of ripple in these configurations, this can encompass a significant fraction of the distribution. In order to quantify this, we have followed a small ensemble of orbits at 40 keV that initially pass through the magnetic axis and have a range of pitch angles: values of $(v_{||}/v)_0$ running from –0.6 to +1 [orbits with $-1 < (v_{||}/v)_0 < -0.6$ are confined in both configurations]. More comprehensive measures of fast particle confinement are under development for these configurations. In Fig. 7 we plot the trajectories for this sample of orbits in Boozer coordinates for both the initial unoptimized configuration and the J^*-optimized configuration. The unoptimized configuration has a loss cone roughly over $-0.2 < (v_{||}/v)_0 < 0.4$. In contrast, the J^*-optimized configuration has no loss cone and confines all of the orbits shown here. In Fig. 8 we examine the confinement properties of the J^*-optimized configuration with increasing energy for a deeply trapped orbit [$(v_{||}/v)_0 = 0.1$] and a co-passing orbit [$(v_{||}/v)_0 = 1.0$] for energies

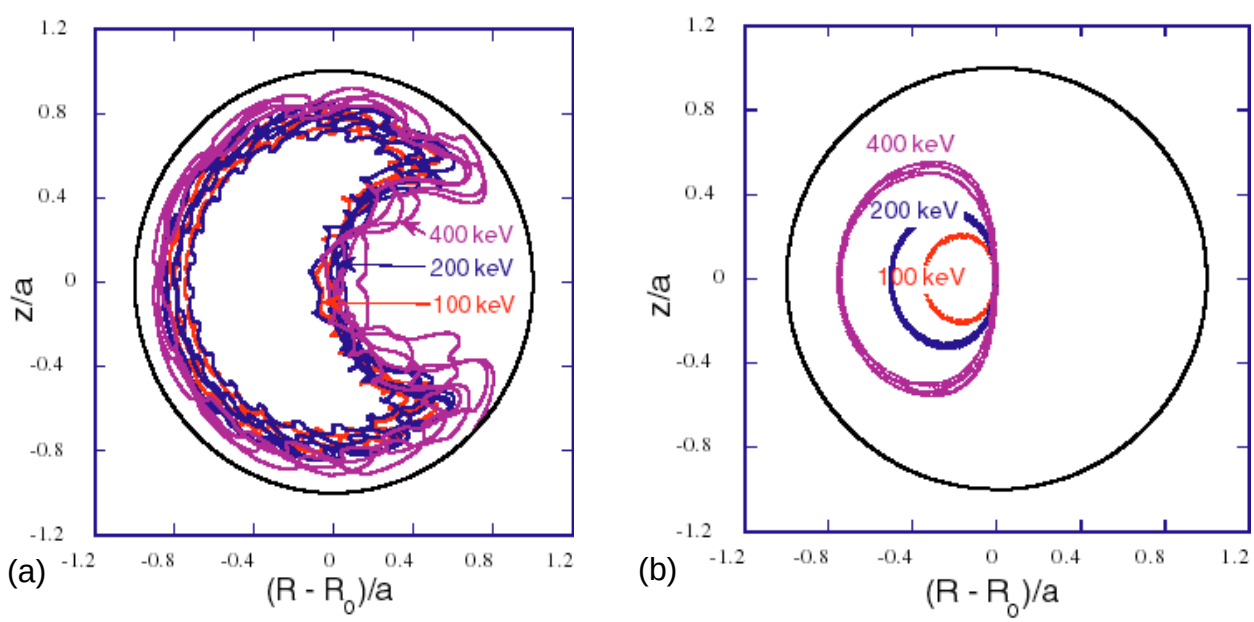

Fig. 8. Energetic ion orbit trajectories in the J^*-optimized configuration for (a) a deeply trapped $v_{||}/v = 0.1$ case and (b) a passing $v_{||}/v = 1.0$ case over a color-coded range of energies (E = 100, 200, 400 keV).

of 100, 200, and 400 keV. The deeply trapped orbit becomes lost at 400 keV, apparently because its drift per bounce has become too large to maintain J^* conservation. The passing orbits are still confined, but with significant displacements away from flux surfaces ($\Delta/a \sim 0.5$). The deeply trapped orbits show an interesting property of confined superbanana stellarator orbit trajectories in that, unlike normal tokamak banana orbits, the orbit width is essentially independent of energy (i.e., because J^* for trapped particles does not depend on energy, in the absence of electric fields). To the extent that J^* is conserved, relatively arbitrary energies will be confined on the same trajectory. The point at which J^* conservation is lost because the drift per bounce becomes too large can be extended by increasing the $\boldsymbol{B}$ field or increasing the device size.

Conclusions

We have developed a new optimization procedure for low-aspect-ratio stellarators that targets bounce-averaged omnigeneity (i.e., minimization of drift away from the flux surface) by aligning contours of the approximate second adiabatic invariant J^* with magnetic flux surfaces. This technique uses the shape of the outermost flux surface and the plasma current profile as control parameters. Our optimization has led to qualitatively new kinds of stellarator configurations that are neither quasitoroidal nor quasihelical. This additional flexibility in the $|\boldsymbol{B}|$ spectrum has opened up the available parameter space at low aspect ratio and resulted in significant improvements in confinement of both thermal and energetic particle components. We hope that such flexibility will allow the inclusion of further criteria [19] related to MHD ballooning stability as well as other potentially important physics issues. The coil reconstruction for these optimized states is relegated to a separate step and appears feasible but will require further development.

Donald A. Spong, Steven P. Hirshman, and John C. Whitson
Oak Ridge National Laboratory
P.O. Box 2009
Oak Ridge, TN 37831-8071 USA

Phone: (423) 574-1307
E-mail: spongda@ornl.gov

References

[1] B. A. Carreras, N. Dominguez, L. Garcia, et al., Nucl. Fusion **28** (1988) 1195.

[2] B. A. Carreras, V. E. Lynch, and A. Ware, *Configuration Studies of a Small-Aspect-Ratio Tokamak-Stellarator Hybrid*, ORNL/TM-13252, June 1996.

[3] D. A. Spong, S. P. Hirshman, and J. C. Whitson, Plasma Phys. Reports **23** (1997) 483.

[4] P. E. Moroz, Phys. Rev. Lett. **77** (1996) 651.

[5] D. W. Ross, P. M. Valanju, H. He, W. H. Miner, P. E. Phillips, J. C. Wiley, A. J. Wootton, and S-B. Zheng, Plasma Phys. Reports **23** (1997) 492.

[6] P. R. Garabedian, Phys. Plasmas **3** (1996) 2483.

[7] J. Nührenberg and R. Zille, Phys. Lett. **A129** (1988) 113.

[8] D. A. Garren and A. H. Boozer, Phys. Fluids B **3** (1991) 2822.

[9] R. N. Morris, C. L. Hedrick, S. P. Hirshman, J. F. Lyon, and J. A. Rome, In *Proc. 7th Int. Workshop on Stellarators, Oak Ridge, TN, April 10–14, 1989*, IAEA, Vienna (1989).

[10] J. R. Cary, C. L. Hedrick, and J. Tolliver, Phys. Fluids **31** (1988) 1586.

[11] J. A. Rome, Nucl. Fusion **35** (1995) 195.

[12] A. A. Skovoroda and V. D. Shafranov, Plasma Phys. Reports, **21** (1995) 937.

[13] J. R. Cary and S. G. Shasharina, Phys. Rev. Lett. **78** (1997) 674.

[14] H. Weitzner, Phys. of Plasmas, **4** (1997) 575.

[15] S. P. Hirshman and J. C. Whitson, Phys. Fluids **26** (1983) 3553.

[16] S. P. Hirshman, J. C. Whitson, and D. A. Spong, "Modular Coil Design for Optimized Stellarators," in preparation.

[17] P. Merkel, J. Comput. Phys. **66** (1986) 83.

[18] R. H. Fowler, J. A. Rome, and J. F. Lyon, Phys. Fluids **28** (1985) 338.

[19] W. A. Cooper, Phys. Plasmas **4** (1997) 153.